

**FUNDAMENTAL PHENOMENA ON FUEL  
DECOMPOSITION AND BOUNDARY-LAYER  
COMBUSTION PROCESSES WITH APPLICATIONS TO  
HYBRID ROCKET MOTORS**

**Semi-Annual Report**

P-31

**Part 1: Experimental Investigation**

Kenneth K. Kuo, Yeu-Cherng Lu, Martin J. Chiaverini,  
George C. Harting, David K. Johnson, and Nadir Serin  
The Propulsion Engineering Research Center  
The Pennsylvania State University  
University Park, PA 16802

NAS 8-39945

**Summary:**

The experimental study on the fundamental processes involved in fuel decomposition and boundary-layer combustion in hybrid rocket motors is continuously being conducted at the High Pressure Combustion Laboratory of The Pennsylvania State University. This research will provide a useful engineering technology base in the development of hybrid rocket motors as well as a fundamental understanding of the complex processes involved in hybrid propulsion. A high-pressure, 2-D slab motor has been designed, manufactured and utilized for conducting seven test firings using HTPB fuel processed at PSU. A total of 20 fuel slabs have been received from the McDonnell Douglas Aerospace Corporation. Ten of these fuel slabs contain an array of fine-wire thermocouples for measuring solid fuel surface and subsurface temperatures. Diagnostic instrumentation used in the test include high-frequency pressure transducers for measuring static and dynamic motor pressures and fine-wire thermocouples for measuring solid fuel surface and subsurface temperatures. The ultrasonic pulse-echo technique as well as a real-time X-ray radiography system have been used to obtain independent measurements of instantaneous solid fuel regression rates.

**Section 1: Test Facility Development**

Figure 1 shows a schematic diagram of the hybrid motor test facility, including a 2-D slab motor analog, a GOX supply system, and an ignition system. The design, construction, and installation of these three subsystems have been completed. In addition, a test rig control system consisting of a

control panel and an IBM PC/AT computer has also been installed and implemented. The details of the motor, GOX supply system, ignition system, and control system are discussed fully in the Quarterly Report dated November, 1994.

The data acquisition system consists of an IBM PC linked to a Nicolet Multipro data acquisition module. The 24 channel Multipro unit records data from two Setra 206 pressure transducers from the GOX supply line, one Setra 205 transducer from the ignition line, several Kistler 601B1 pressure transducers from the motor, an E-type thermocouple from the GOX supply line, and an array of embedded S-type thermocouples from the fuel slab. The acquisition system also stores data from a Panametrics Videoscan ultrasonic transducer used for deducing instantaneous fuel regression rate.

The block diagram showing major components of the ultrasonic pulse-echo acquisition system for instantaneous regression rate measurement is given in Figure 2. An ultrasonic transducer is placed behind the top fuel slab within the fuel sample holder. The transducer, which can be placed in any one of four locations, both emits and receives the ultrasound signal. The transducer is connected directly to the Electronic Device for Ultrasonic Measurement (EDUM). An oscilloscope provides a real-time visual record of the ultrasonic transducer signal. At the same time, this signal is recorded by the Nicolet Multipro Transient Analyzer. The ultrasonic signal, expressed in millivolts, measures the variation in propagation time of an ultrasound pulse through the fuel sample. As the fuel regresses, the propagation time of the ultrasound pulse continuously decreases due to a decrease in fuel web thickness.

An X-ray radiography system is also used to obtain instantaneous fuel thickness information. As shown in Figure 3, an X-ray tube head emits high intensity photons. These photons pass through the LEXAN/MXB-360 windows of the motor and then impinge on an image intensifier. Inside the motor, a portion of the X-ray photons passing through the fuel slab region is absorbed by the solid fuel; however, most of the X-ray photons passing through the port area experience little absorption. Because of this difference in the attenuation of the X-ray photons, the X-ray images display contrasting bright and dark regions, which indicate the port area and fuel slabs, respectively. The fuel regression rate can then be deduced from these images.

In order to obtain the average fuel regression rate, the fuel slabs are

weighed before and after each test. Using a micrometer, the axial profiles of the fuel slabs are also recorded before and after each test, giving a measure of the variation of time-averaged regression rate with axial location.

## Section 2: Test Results

Table 1 below summarizes the test conditions of seven firings conducted thus far. The pressure ranges given in the second column correspond to the quasi-steady peak pressure of the motor to the motor pressure before shut down. The pressure drop for most test runs was mainly due to erosion of the nozzle. The third column gives the initial GOX mass flux found by dividing the known GOX mass flow by the initial combustor port area. Test no. 004 has a high maximum pressure due to a partial blockage of the nozzle by a piece of solid fuel torn from the fuel slab.

Table 1. Summary of seven test firings

Test no.	Pressure (psia)	$G_{ox,0}$ (lb/in <sup>2</sup> -s)	Test duration (s)
001	1240-335	0.48	15.0
002	300-300	0.097	2.7
003	500-360	0.178	3.6
004	1300-260	0.237	5.8
005	770-410	0.225	4.1
006	565-195	0.211	6.4
007	530-250	0.148	9.0

### Section 2.1: Motor Operating Pressure

Figure 4 shows a pressure-time trace of the hybrid motor during Test 002. The initial jump in pressure at about 0.2 seconds was caused by the start of GOX flowing through the supply line and into the motor. At a time of approximately 1.5 sec., the onset of ignition was achieved and flame began to spread over the solid fuel. Within about 0.5 seconds the chamber filling process is finished. At about 2.0 seconds after the start of the test, the motor reaches a quasi-steady state operating condition of about 300 psia. During this period significant pressure oscillations, on the order to  $\pm 20\%$  of the mean

pressure, occur. At about 4.3 sec., the GOX flow is shut off and the nitrogen purge is activated. The total time of combustion for this run is about 2.5 seconds. Figure 5 shows the frequency spectrum of the pressure oscillations. The first mode of oscillation occurs at a frequency of about 55 Hz, with a second mode at 110 Hz.

Figure 6 shows the pressure-time trace for Test 003. This test was conducted at a higher chamber pressure (500 psia) and for a longer duration (3.5 sec.) than Test 002. Even stronger oscillations were observed at the beginning of the test run. The decay in mean operating pressure is due to erosion of the graphite nozzle.

Figure 7 shows the pressure-time trace for Test 005. In order to isolate the cause of the pressure oscillations observed in the previous tests, a section of steel tubing in the GOX supply line between the venturi and the motor inlet was replaced by a new section containing a 360° loop approximately 16 in. in diameter. It was initially surmised that increasing the length of this section would only reduce the frequency of the pressure oscillations. The oscillatory frequency was indeed reduced, but as shown in Fig. 7, the amplitude of the oscillations was reduced as well. Except for a few spikes in Test 005, the pressure oscillations were below  $\pm 15\%$  of the quasi-steady mean pressure. Figure 8 shows the frequency spectrum of the oscillations. The frequency of the first mode is around 40 to 50 Hz, with a secondary mode at about 90 Hz. Note also that the amplitude of these oscillations is much lower than those of Test 002 (shown in Fig. 5).

Figure 9 shows the pressure time trace of the motor for Test 006. In this case, a 2 inch-long orifice with an area blockage ratio of 65% was inserted in the GOX line just upstream of the motor entrance. This long orifice successfully damped out nearly all of the pressure oscillations observed in the previous tests. Though the quasi-steady mean pressure drops markedly during the test run due to nozzle erosion, the pressure oscillations are only about  $\pm 1\%$  of the mean pressure during this test.

## Section 2.2: Solid Fuel Temperature

Figure 10 shows a temperature-time trace for Test 005. This data was obtained using a 25  $\mu\text{m}$  fine-wire Pt/Pt-10%Rd thermocouple located 11.5 in. from the leading edge of the upper fuel slab. The thermocouple registers ambient temperature for the first six seconds of the test then begins to register

higher temperatures as the fuel surface regresses toward the thermocouple junction location. The temperature profile increases smoothly until a temperature of around 950 K is reached. Here, the profile assumes a rough, jagged shape, implying that the fuel surface has regressed beyond the thermocouple junction location, exposing it to the gas-phase region. The thermocouple was destroyed when it reached a temperature of around 1700 K. According to the Omega Co. Temperature Handbook, the maximum temperature sustainable by the S-type thermocouple is around 1750 K.

Figures 11 and 12 show similar results for Test 006. Note that in Figure 11, the graph displays several temperature plateaus between 4.25 and 4.5 seconds. The first plateau corresponds to a temperature of about 950 K, which is slightly lower than the surface temperature measurement of Test 005 (see Fig. 10) which was conducted at a higher pressure. The next step occurs at a temperature of about 1200 K. This temperature plateau is believed to be associated with the passage of the thermocouple junction through a surface melt layer of liquefied fuel.

Figure 12, which shows the temperature-time trace of the same test measured by an S-type thermocouple located 17.5 in. from the leading edge of the fuel slab surface, where the boundary layer is turbulent. Comparing this trace with the upstream one (shown in Fig. 11), it is apparent that the surface heat feedback from the gas phase is much stronger for the turbulent boundary-layer zone due to increasing mass flux in the axial direction. Thus, the thermal profile in the subsurface region is steeper. Corresponding to the higher energy feedback, the surface regression rate toward the rear of the fuel slab was higher than that of the front section.

The recovered fuel surfaces also exhibit the transition from laminar to turbulent boundary layer with very distinct roughness patterns shown in Figure 13(a) through (c). In the upstream region, the solid fuel has a very smooth surface due to melt layer coverage. In the transition region surface ripples running in the transverse direction are clearly visible. In the downstream turbulent region, the surface roughness is greater in magnitude with a more random pattern. Due to the high rates of heat feedback, the melt layer may or may not exist in the turbulent region. The solid fuel could readily pyrolyze into gas-phase products without going through a liquefaction process.

Figures 14 and 15 compare the fine-wire thermocouple traces at upstream

( $x=2.5''$ ) and downstream ( $x=20.5''$ ) locations of the top fuel slab for Test 007. Again, the temperature profile recorded by the upstream thermocouple shows a much thicker thermal wave than that of the downstream thermocouple. The surface temperature in the upstream location is lower than that of the downstream location. Correspondingly, the fuel slab at the upstream location has a lower regression rate than that of the downstream.

### Section 2.3: Solid Fuel Regression Rate Measurements

Figure 16 shows the bottom fuel slab profile before and after firing for Test 006. (The top fuel slab profile is similar to the bottom since the buoyancy effect is negligible in this forced convection dominated test condition). Except near the leading edge of the fuel slab, the web thickness of the recovered sample decreases along the fuel slab in the axial direction. This result is consistent with the fact that the total mass flux along the motor increases with distance along the slab, leading to a higher regression rate. Following the increase in mass flux, the heat transfer rate increases along the solid fuel slab, resulting in the increases of regression rate. The leading edge of the fuel slab has a relatively high regression rate because the flame zone in the boundary layer is very close to the fuel surface in the very upstream region, where the boundary layer thickness is very thin. The high regression rate at the trailing edge is believed to be caused by the recirculating flow before the entrance of the aft mixing chamber. The average regression rate found by measuring the average web thickness burned over the test time is about 0.878 mm/s, while a value of about 0.88 mm/s is obtained by weighing the fuel slab before and after each test.

Figures 17 through 19 show a set of images obtained using the X-ray radiography system for Test 007. Figure 17 shows a cross-sectional view of the interior of the chamber at the start of GOX flow. GOX flow is from left to right, and the image covers a length of about 2.75 in., beginning at a point 5 in. downstream from the leading edge of the fuel slab. The dark band running vertically across the image is a 0.25 in diameter section of steel tube placed on the outside of the chamber. This tube is used to set a scale on the image. Figure 18 shows the same region 5 seconds into the test, and Figure 19 shows fuel surface locations at the end of the test. All three images clearly show the chamber port and the edges of the top and bottom fuel slabs.

The average regression rate found by weighing the fuel slabs before and

after the test was about 0.75 mm/s for Test 007. By analyzing the X-ray images, an instantaneous regression rate was found to be around 0.79 mm/s over the majority of the test time, except for ignition and shutdown transients.

### Section 3: Future Work

Full duration tests will continue to be conducted under various operating conditions using several data acquisition systems described above. A more complete data processing procedure will be developed, including the computer routine for deducing regression rate from ultrasonic signals. In addition to the HTPB fuels processed at PSU, the fuel samples from the McDonnell Douglas Aerospace company will be utilized in a series of tests.

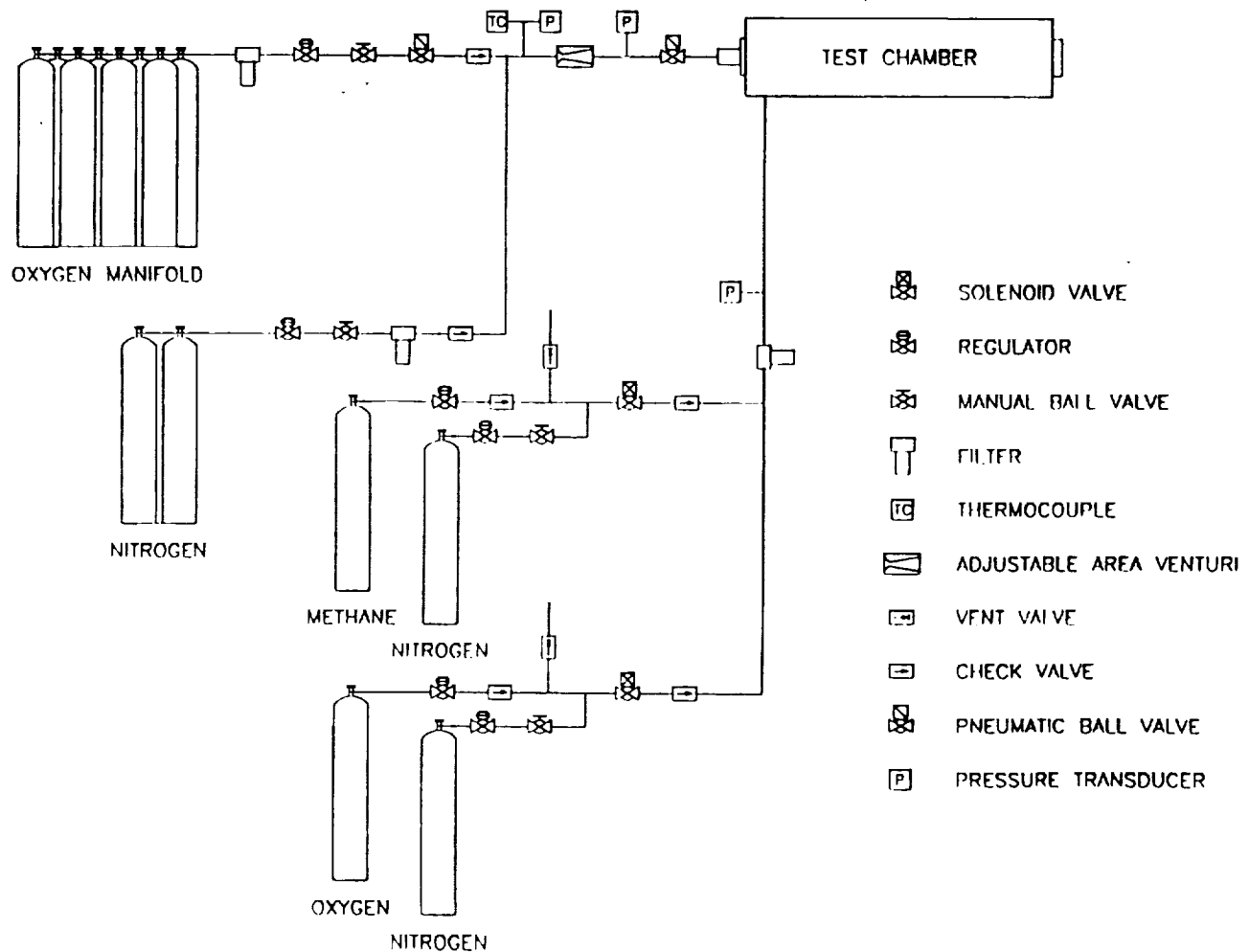


Figure 1. Schematic Diagram of Hybrid Motor Test Facility.

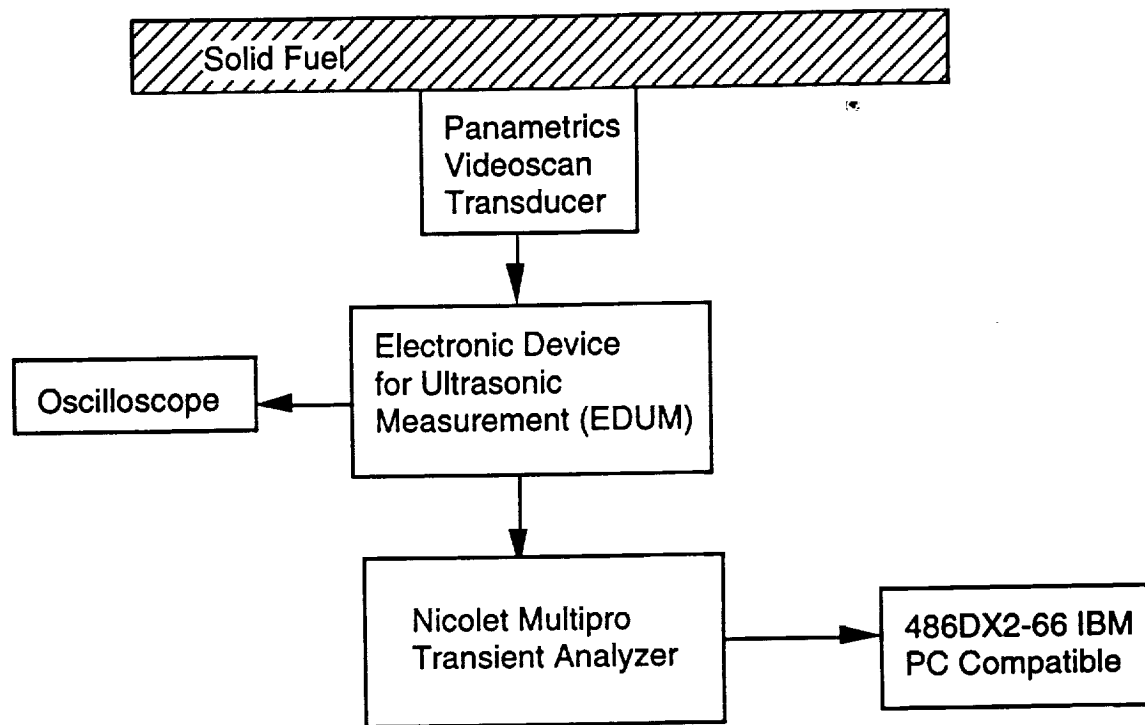


Figure 2. Block Diagram for Ultrasonic Pulse-Echo System

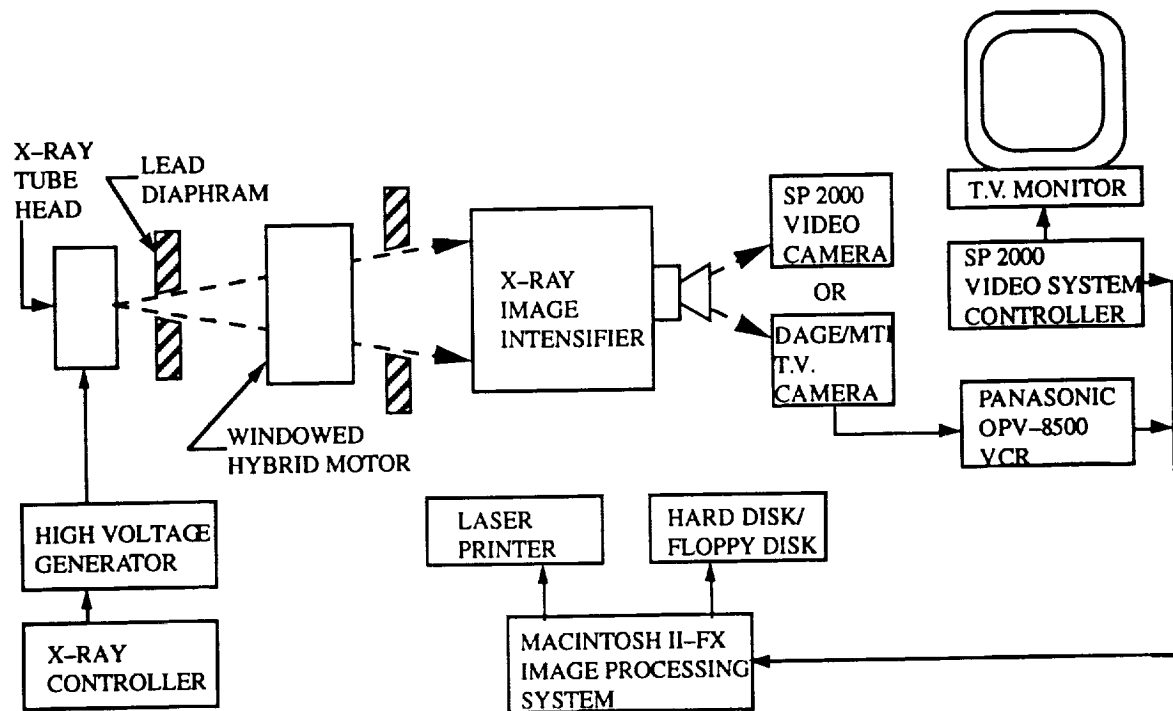


Figure 3. Block Diagram for Real-Time, X-Ray Radiography System



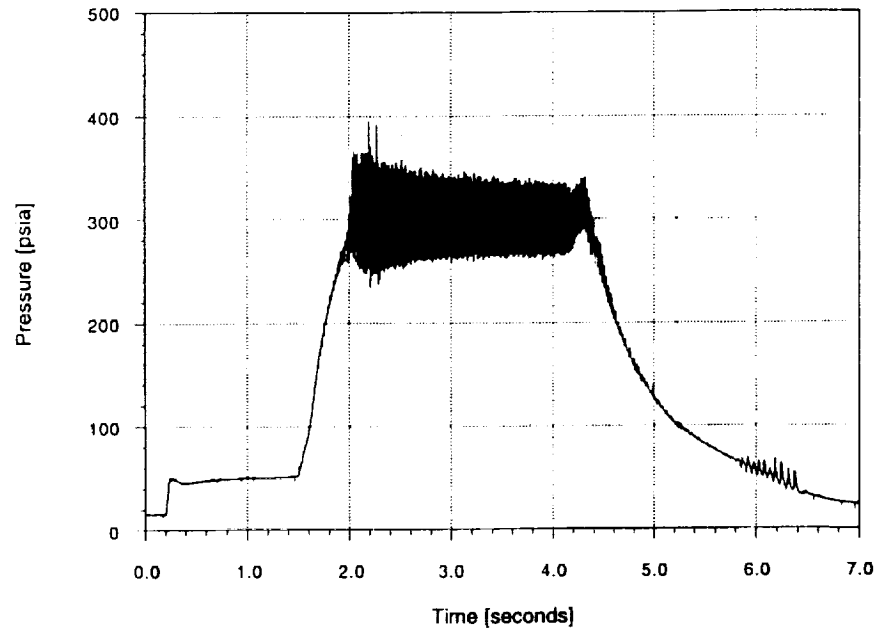


Figure 4. Motor pressure-time trace from Test 002.

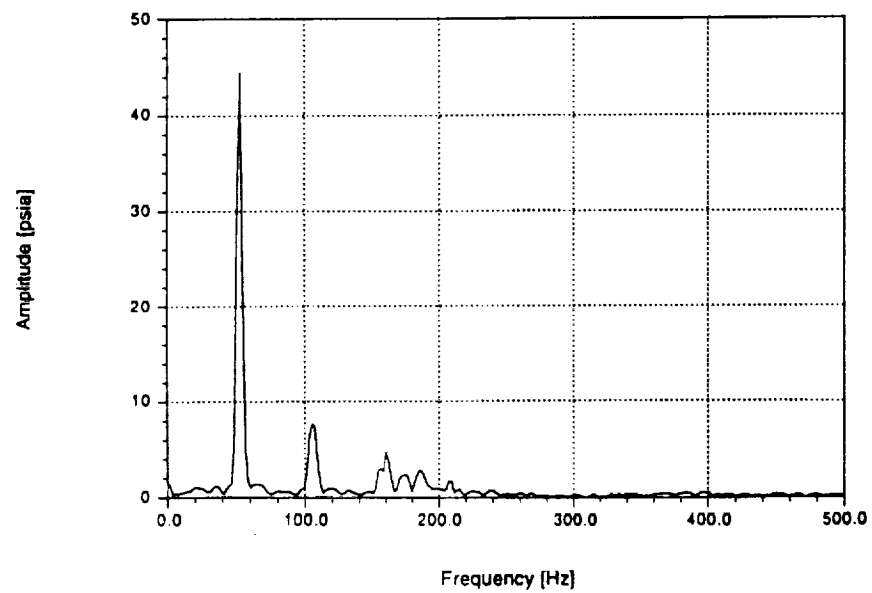


Figure 5. Frequency spectrum analysis of pressure-time trace of Test 002.

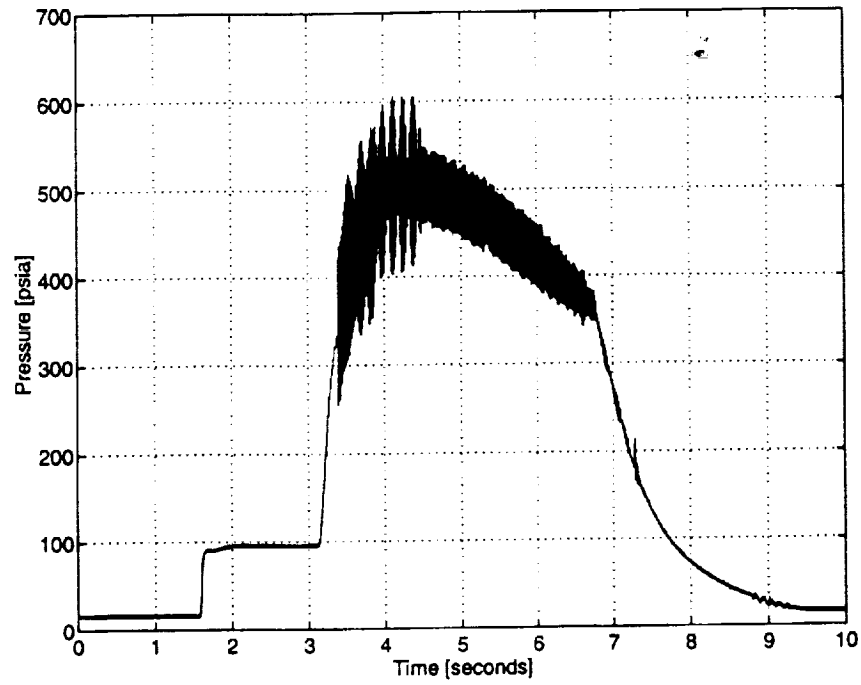


Figure 6. Motor pressure-time trace from Test 003.

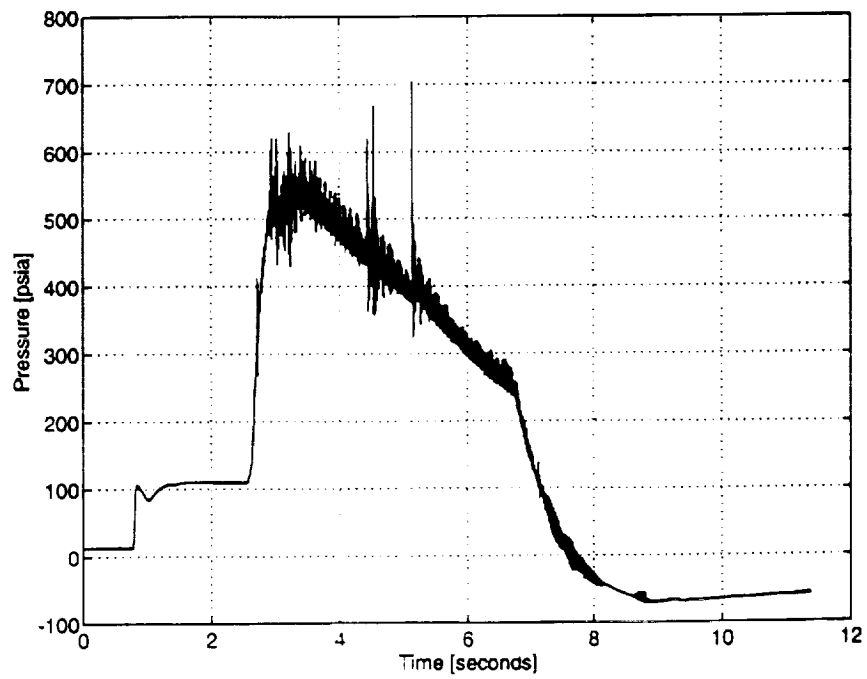


Figure 7. Motor pressure-time trace from Test 005.

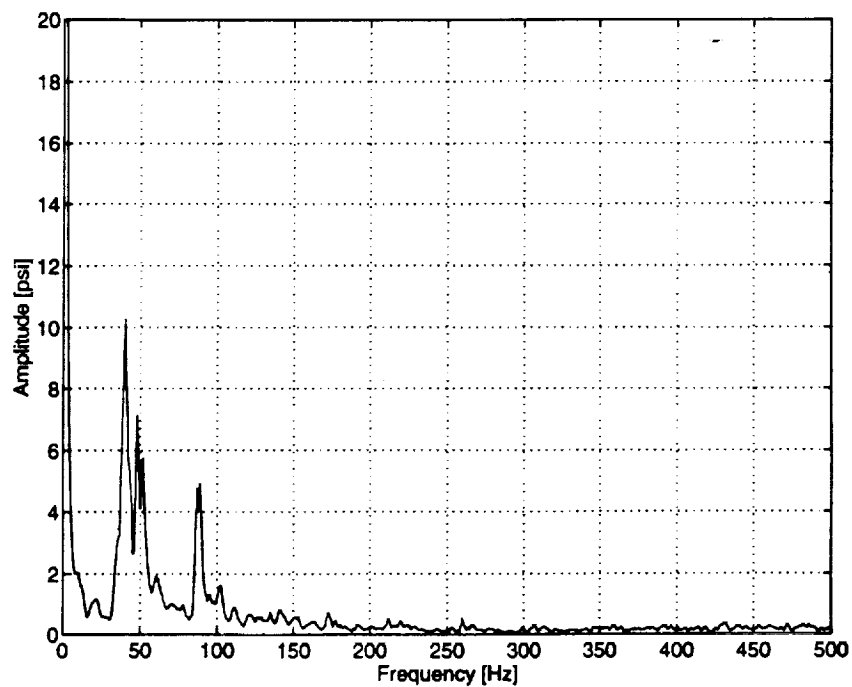


Figure 8. Frequency spectrum analysis of pressure-time trace of Test 005.

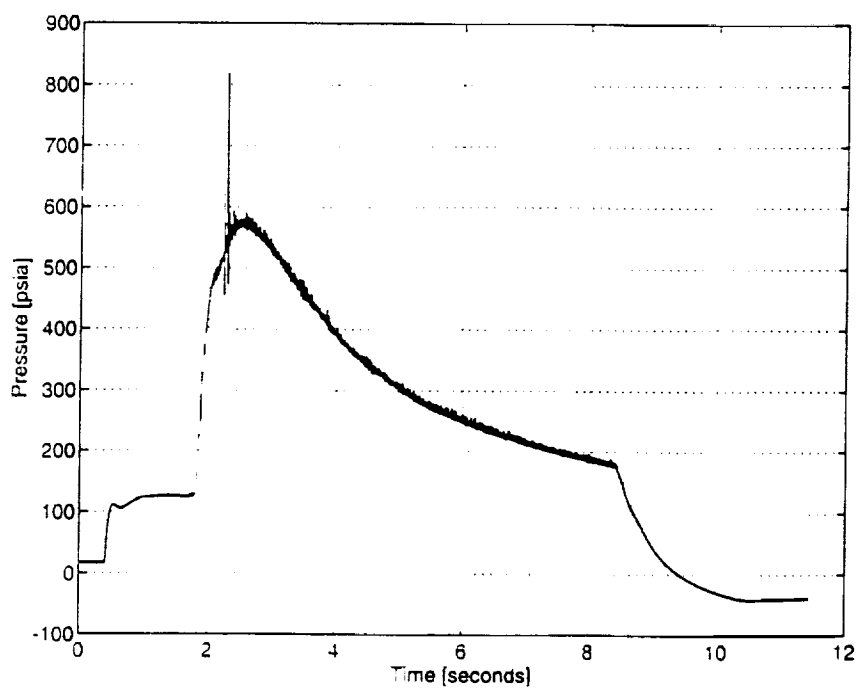


Figure 9. Motor pressure-time trace from Test 006.

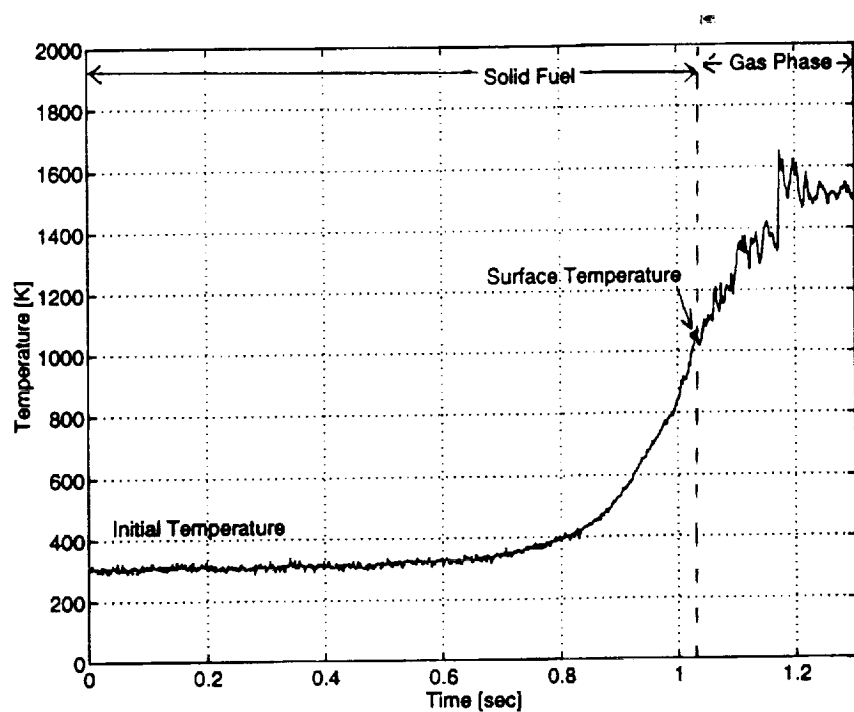


Figure 10. Temperature-time trace for Test 005.

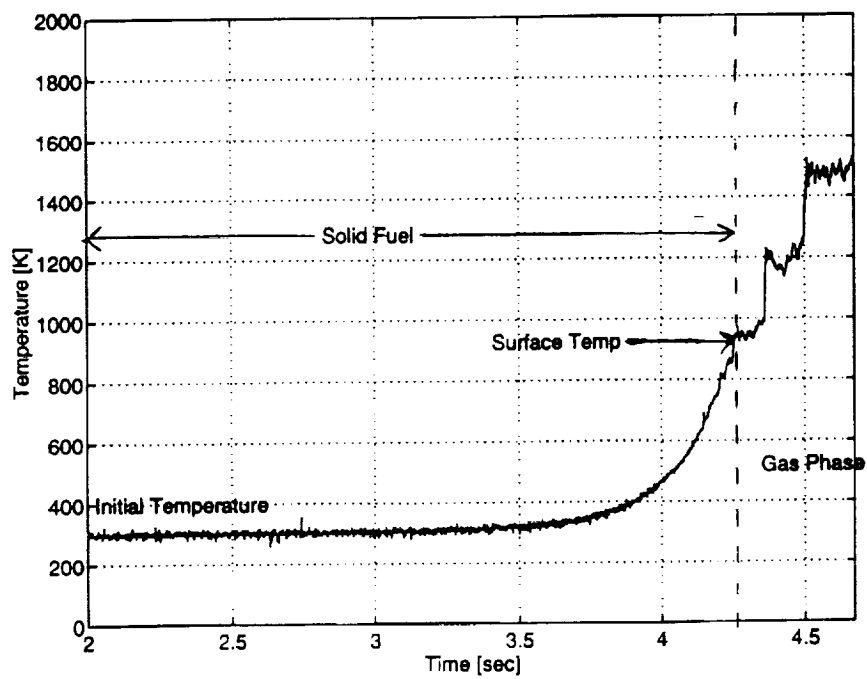


Figure 11. Upstream temperature-time trace for Test 006.

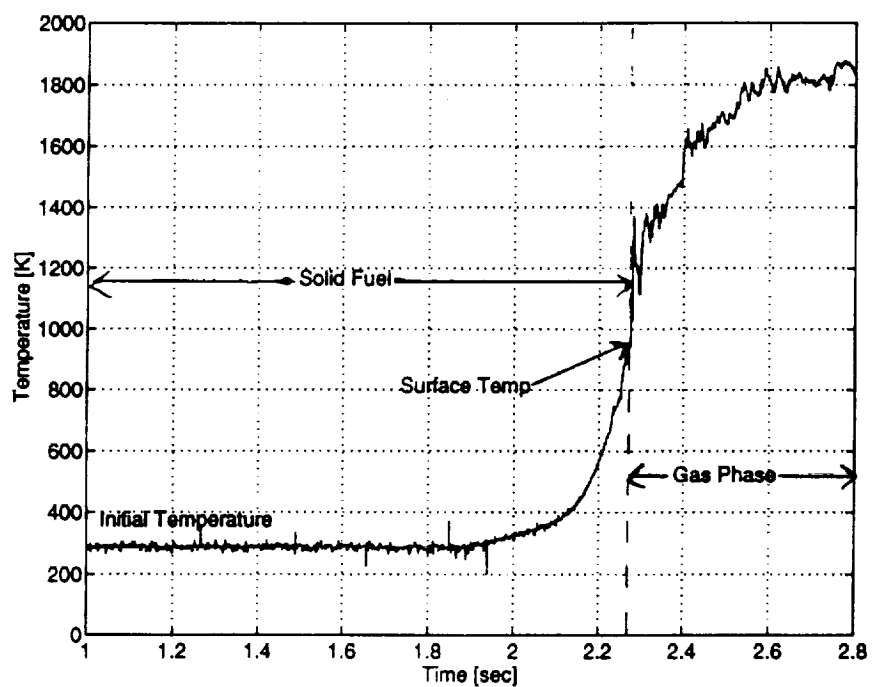
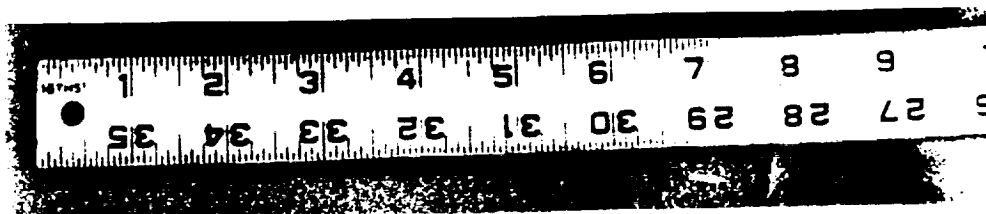
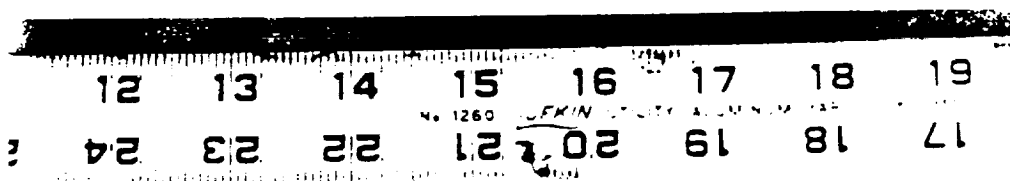
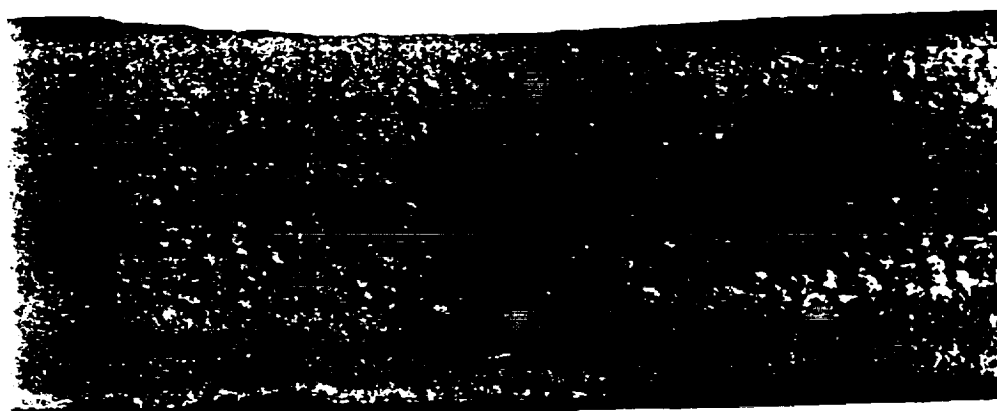


Figure 12. Downstream temperature-time trace for Test 006.

- Very smooth surface
- Surface seems to be covered by melt layer
- The leading edge region has some tiny holes corresponding to high heat fluxes



- Distinct transition from smooth to rough surfaces
- This transition is caused by the change from a laminar to turbulent boundary layer
- Fuel surface for turbulent boundary layer was not covered by melt layer due to high heat flux



- The edge regions have 3-D effect
- The regression rate in the fuel width direction seems to be uniform

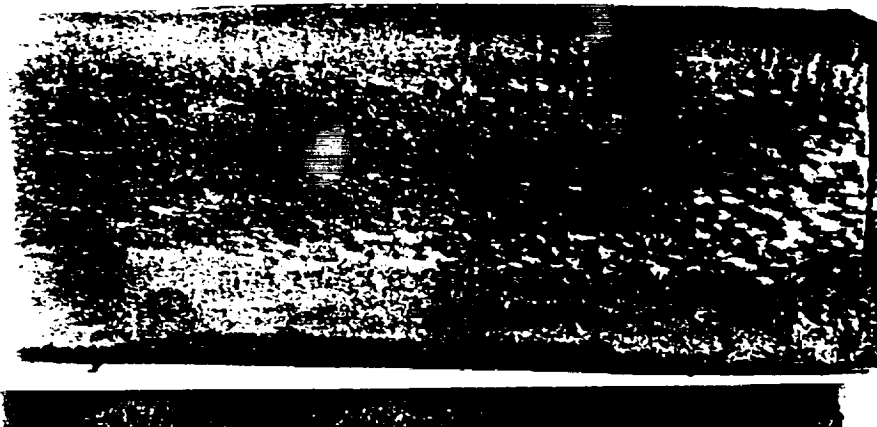


Figure 13. Photographs of recovered solid-fuel slabs after Test 003.

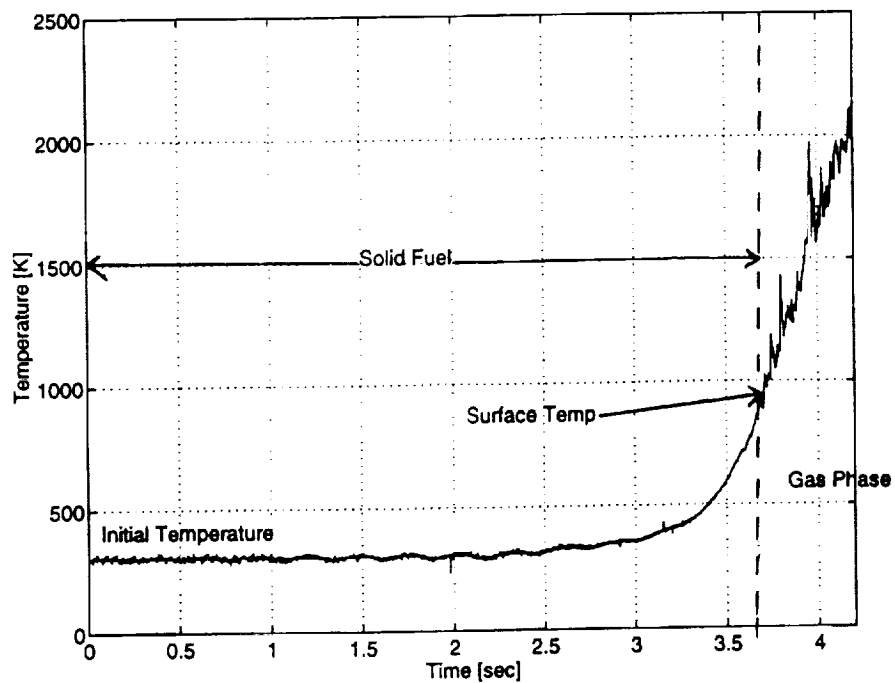


Figure 14. Upstream temperature-time trace for Test 007.

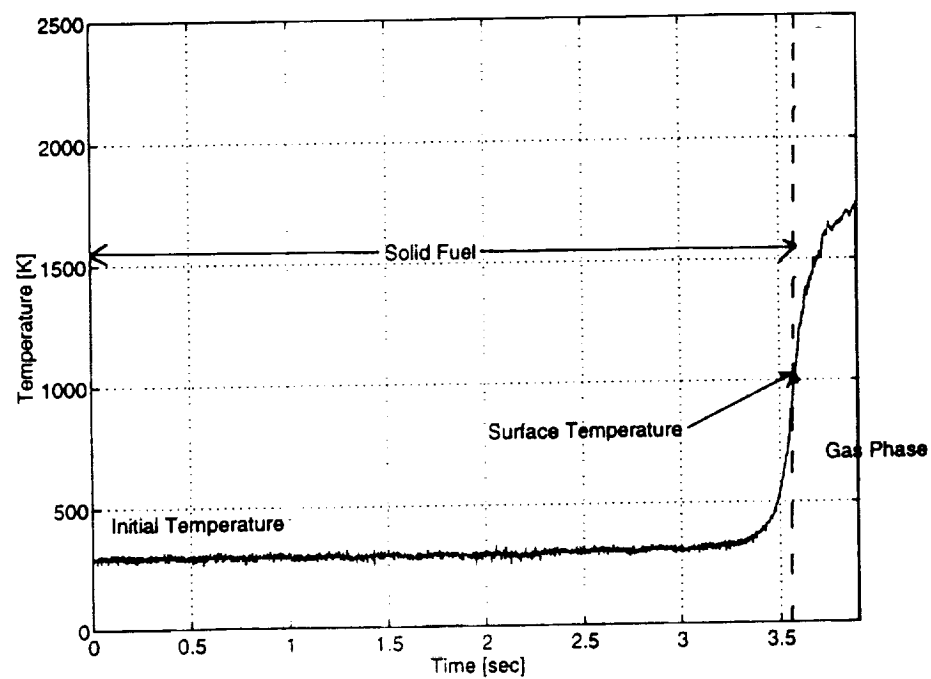


Figure 15. Downstream temperature-time trace for Test 007.

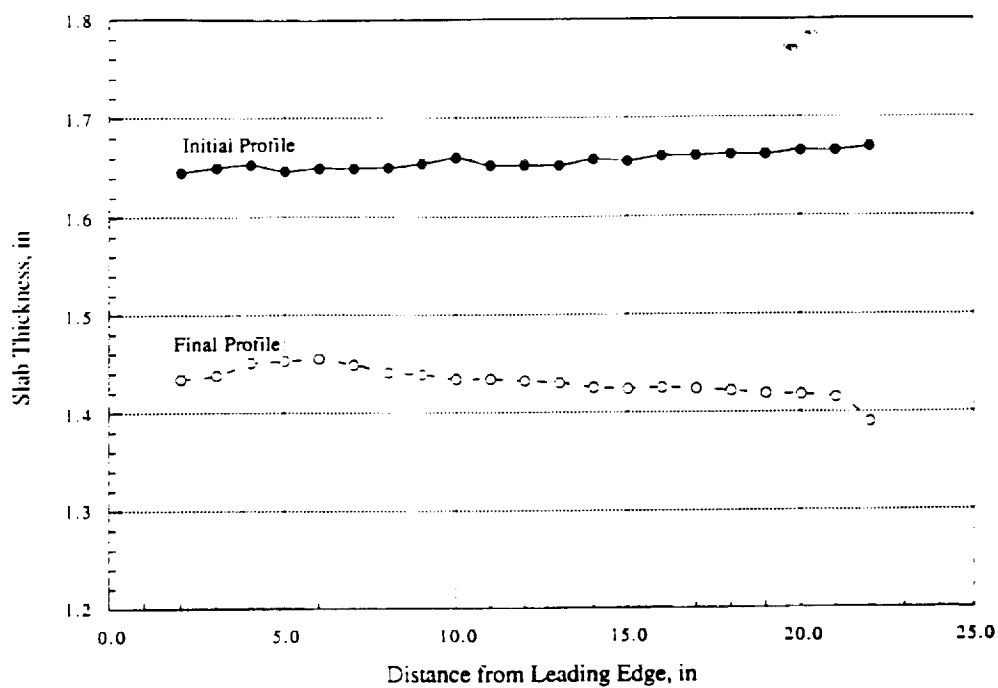


Figure 16. Thickness of the bottom fuel slab before and after Test 006.

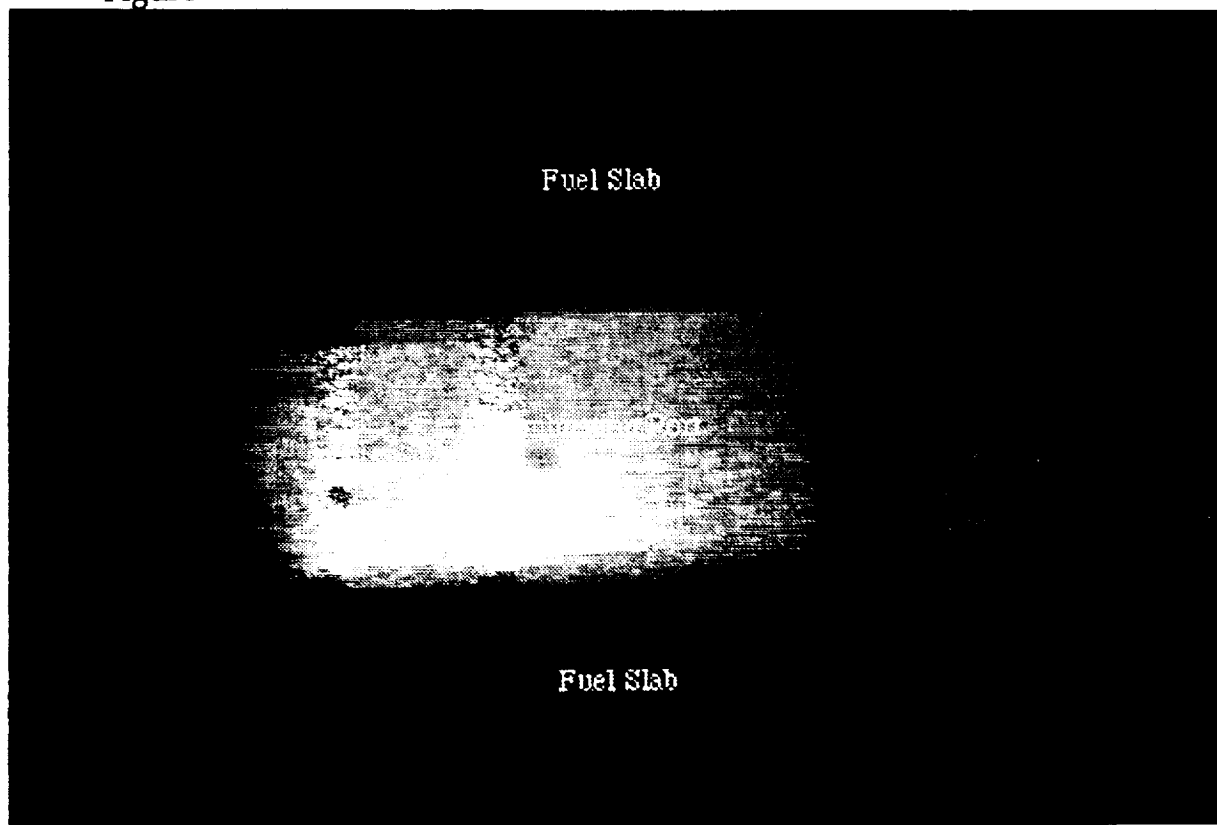


Figure 17. X-ray image from Test 007 at start of GOX flow.



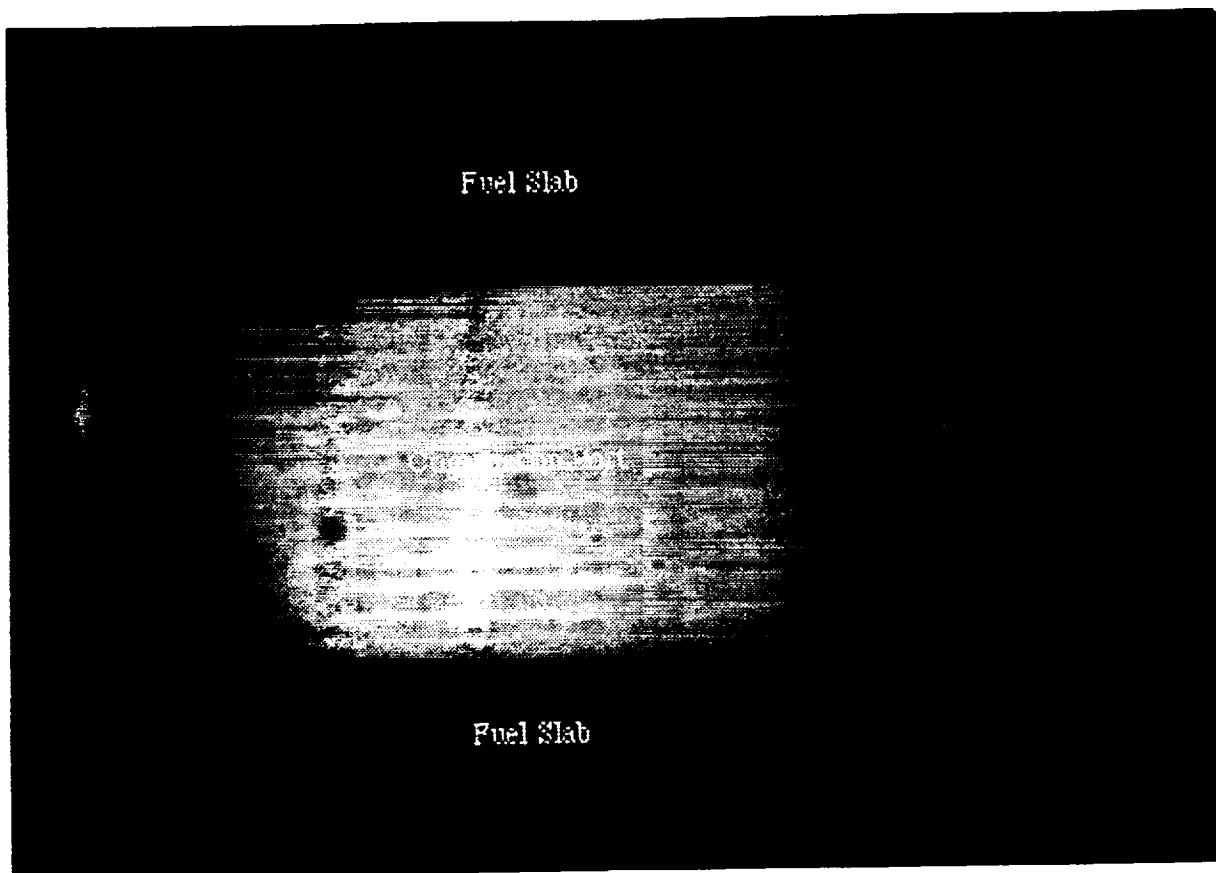


Figure 18. X-ray image from Test 007 after 5 seconds.

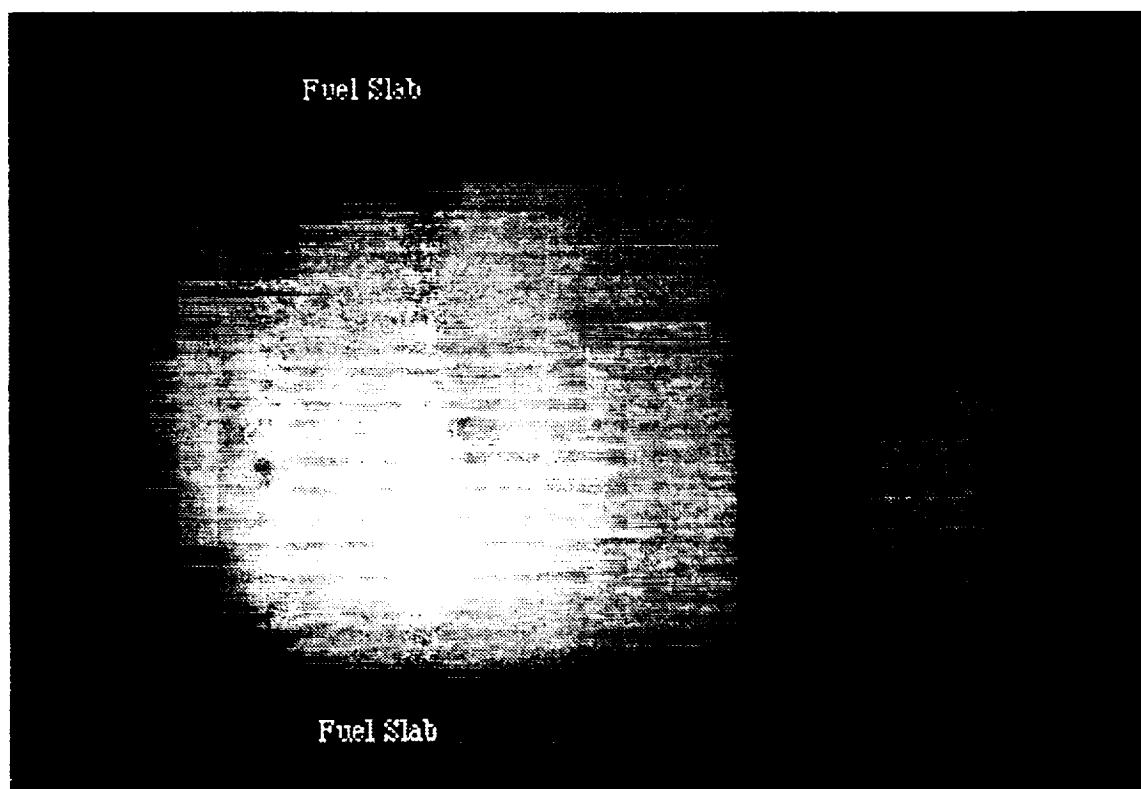


Figure 19. X-ray image from at the end of Test 007.

ORIGINAL PAGE IS  
OF POOR QUALITY

**Fundamental Phenomena on Fuel Decomposition  
and Boundary Layer Combustion Processes  
with Applications to Hybrid Rocket Motors**

**Semi-Annual Progress Report  
November 1, 1994-April 30, 1995**

**Task 2: Theoretical Investigation  
C. L. Merkle and S. Venkateswaran**

## **1. Introduction**

The primary effort in the present reporting period was concerned with parametric studies of the experimental slab burner configuration with HTPB as fuel and GOX oxidizer. Solutions have included the full-length geometry in order to perform detailed characterization of the fuel surface regression rates. Comparison with available data from previous small-scale tests suggest that radiative fluxes contribute significantly to the energy balance on the fuel surface, and when these are accounted for, reasonably good agreement between predictions and measurements is obtained. Further, the computational solutions, for different GOX flow rates, chamber pressures and stages in the burn, reveal trends that are in qualitative agreement with experimental observations.

The present report is organized as follows. We first present the details of the computational model including the coupled solid/gas-phase formulation and the radiative transfer model used. This is followed by representative computational results of the slab burner configuration including the aft-nozzle section. We then present a summary of some of the parametric studies and compare the predicted surface regression rates with available data. Finally, we outline our plans for the future months.

## **2. Computational Model Formulation**

The gas-phase computational model involves the solution of the Favre-averaged Navier-Stokes equations coupled to species transport and turbulence equations. The  $k-\epsilon$  turbulence model is used along with the Chien low Reynolds number model for near

wall effects. The combustion in the gas phase is treated using two-step global chemistry. Radiative transfer in the gas-phase is treated using the diffusion approximation valid for optically thick media, as described later. For the solid-phase, the pyrolysis of the solid fuel is represented through an Arrhenius rate equation. Butadiene is taken to be the only gaseous product of the pyrolysis of HTPB. The coupling between the gas and solid phases is accomplished through the interfacial boundary condition which is described below.

## 2.1 Coupled Solid/Gas Phase Formulation

The coupling between the solid and gaseous phases is effected through the interfacial boundary condition. Because the exact details of the solid-phase reactions are not well-understood, this process needs to be modeled in empirical fashion. Previous modeling efforts have generally assumed pyrolysis of the HTPB fuel and have represented this process by means of an Arrhenius-type reaction. We are similarly adopting this approach and are using activation energies obtained from the literature. Accordingly,

$$\rho_s r_b = A_s \exp\left(\frac{-E_a}{R_u T_s}\right) \quad (1)$$

where  $T_s$  represents the interface temperature which is to be determined as part of the solution. The interfacial energy balance is given by:

$$-\lambda \frac{\partial T}{\partial y} + Q_{rad} + \rho v h - \sum_{i=1}^N \rho D_{im} \frac{\partial Y_i}{\partial y} h_i = -\lambda_s \left( \frac{\partial T}{\partial y} \right)_s - \rho_s r_b h_s \quad (2)$$

where the left side of this equation represents the gas-phase quantities and the right side represents the solid-phase quantities. The first term on the left is the convective heat flux to the wall, while the second term is the total radiative heat flux. The modeling of the radiation is described in the next section. The two relations are augmented by a closed form solution for locally one-dimensional thermal conduction in the solid:

$$T(y) = T_\infty + (T_s - T_\infty) e^{-r_b / \nu_{ts} y} \quad (3)$$

where  $T_\infty$  is the temperature of the unheated fuel, and  $\nu_{ts}$  is the thermal diffusivity of the fuel slab. The derivative of Eqn. (3) may be substituted into Eqn. (2) to determine the conduction heat loss in the solid phase. Thus, by combining Eqns. (1), (2) and (3), both the fuel surface temperature  $T_s$  and the surface regression rate  $r_b$  may be

determined. The wall blowing rate is then given by applying a mass balance at the interface:

$$\rho v = -\rho_s r_b \quad (4)$$

For the gas-phase boundary condition, the above set of relations is augmented by the standard non-slip axial velocity, the normal momentum equation (for the interface pressure) and the appropriate species balances (for the species mass fractions  $Y_i$ ).

## 2.2 Radiative Transfer Model

Measurements of radiative flux in the JPL small-scale hybrid thruster tests have revealed that radiation for the gas/soot may account for up to 30 % of the total surface heat flux. Thus, radiation may play an important role in the determination of the fuel surface regression rates. Detailed modeling of radiation is difficult and computationally expensive. For these reasons, we have implemented a simple radiative transfer model which accounts for both molecular radiation from the gas as well as radiation from soot particles in the flame. For molecular gas radiation, the optical path lengths in the medium are likely to be small (less than unity). It is then possible to treat them using the optically thin approximation, which may be written as:

$$Q_{\text{rad}} = \sum_{i,j} \frac{4\sigma k_{ij} T_{ij}^4}{J_{ij}} \mathcal{F}_{ij-k}$$

where  $1/J_{ij}$  is the volume of the  $(i,j)^{\text{th}}$  cell and  $\mathcal{F}_{ij-k}$  is the view-factor of that cell with respect to the  $k^{\text{th}}$  grid location on the fuel slab surface.

On the other hand, radiation from soot particles is likely to be much stronger and the associated optical path lengths would be much greater than unity. In this optically thick limit, it is possible to represent the radiative flux using the diffusion approximation:

$$Q_{\text{rad}} = -\lambda_R \frac{\partial T}{\partial y}$$

where  $\lambda_R = \frac{4}{3}\pi \frac{C}{k} T^3$ . Specification of the gas absorption co-efficients would require a model for soot concentration in the flame. This is currently being implemented. In the calculations performed so far, the absorption co-efficients are selected so as to provide radiative fluxes of about 30% of the total heat flux, in accordance with the JPL measurements mentioned earlier.

### 3. Computational Results

#### 3.1 Representative Solution

We present some representative computational solutions of the experimental slab burner configuration. Figure 1 shows the physical configuration mid-way through the burn. The top figure shows the configuration to scale while in the other plots the  $y$ -coordinate has been exaggerated to clarify the details of the flowfield. The size of the grid is 101 X 61. The axial clustering of grid cells signifies the leading edge of the fuel slab. Strong wall-stretching is employed to resolve the turbulent boundary layer adequately—important for accurate wall heat flux predictions. In the cases shown, the details of the forward-facing step at the head-end of the fuel slab and the backward-facing step at the aft-end have been omitted since the primary purpose of the present calculations is to characterize the fuel surface regression rates. The bottom figure shows the temperature contours for a chamber pressure of 30 atm and a GOX flowrate of 0.8 lbm/s. The peak temperature is 3500 K. The flame is seen to start at the fuel surface near the leading edge of the fuel slab, where the oxidizer and pyrolyzed fuel first come into contact. Further downstream, the flame moves outward as the oxidizer is consumed. For the case shown, the flame does not reach the centerline; however, the oxidizer core does get heated by the flame through thermal diffusion and turbulent mixing.

Figure 2 shows corresponding contours of axial velocity, carbon-dioxide and GOX mass fractions. The velocity contours show rapid acceleration of the gases because of the expansion of the hot products of combustion. Specifically, the boundary layer develops very quickly first because of the displacement effect introduced by the flame, then by the diffusive heating of the core gas and eventually due to the mass addition effect of the pyrolyzing fuel. These observations bring into question the application of boundary layer theory to represent the hybrid combustion process, a procedure that has been frequently applied in previous analyses. The carbon dioxide mass fraction in Fig. 2 outlines the location of the flame, while the GOX mass fraction indicates a GOX-rich core, which means that the oxidizer is not completely consumed. The mass fractions also reveal the classic diffusion flame scenario with flame zone separating the fuel from the oxidizer. It is therefore apparent that downstream mixing would be crucial to maximizing combustion efficiency. Future calculations will address this issue parametrically.

The fuel surface regression rate, temperature and heat fluxes are given in Fig. 3. The surface regression is observed to be moderately dependent on axial location and

varies between 0.01 and 0.04 in/s. The corresponding surface temperature ranges from 950 to 1050 K approximately. The convective and radiative heat fluxes show the same trends. As mentioned earlier, the radiative properties have been calibrated so that the radiative fluxes are about 30% of the total wall heat flux. Figure 4 shows the variation of the mass flux ( $G = \rho u$ ) along the centerline of the channel at three different stages in the burn. It is clear that the mass flux varies quite significantly and in a complex fashion depending on the axial location and the stage in the burn. This is because of the heating effects on the density and velocity of the core gases. Again, it is evident that the traditional boundary layer assumptions will not hold for the fluid dynamics in the hybrid rocket combustor.

### 3.2 Characterization of Regression Rate

Detailed parametric characterization of the fuel surface regression rates have been carried out with and without radiation effects. Calculations have been carried out for chamber pressures between 20 and 60 atm, GOX flowrates between 0.2 and 0.8 lbm/s and at several stages in the burn. The computational results thus provide a comprehensive database for the experimental conditions. In this section, we summarize some of these results and compare the predicted regression rates with available data from previous small-scale tests.

Figure 5 shows temperature contours corresponding to three different stages in the burn for a chamber pressure of 30 atm and a GOX flow rate of 0.8 lbm/s. As the burn progresses, the GOX mass flux ( $G = \rho u$ ) decreases because of the increase in the cross-sectional area of the channel. This in turn results in lower wall heat fluxes and slower surface regression rates as evident in Figs. 6 and 7. Here, results are shown for both the case wherein only convective fluxes are considered (Fig. 6) and for the case with convection and radiation considered (Fig. 7). It is observed that inclusion of the radiative fluxes results in noticeably higher regression rates even though the qualitative trends remain the same. The temperature contours in Fig. 5 likewise show slower combustion rates and less bulk-gas heating as the burn progresses, a reflection of the decrease in regression rates of the fuel slab.

Comparison of the predicted regression rates with available data is shown in Fig. 8, where the regression rate is plotted against the head-end GOX mass flux,  $G$ . The experimental data included in this figure are from small-scale tests performed at JPL, General Dynamics-Thiokol-Rocketdyne (G-T-R) and ONERA. The JPL results are for GOX flow rates that are an order magnitude lower than the G-T-R data, while the ONERA results are for HTPB/air rather than HTPB/GOX. The computational

results are plotted alongside the experimental data in two sets—with and without radiation. It is seen that regression rates are underpredicted when only convective fluxes are considered. Inclusion of radiation ensures more realistic regression rates and the predicted data agree well with the G-T-R data. The close agreement is, however, somewhat coincidental since the present radiation model is simplified and also because the experimental results are averaged regression rates for a complete firing, while the computed results are for a given stage in the burn. However, it is encouraging that the computed results present a reasonably accurate picture of the hybrid combustion process. More detailed validation of fuel surface temperature and regression rates will be possible with the results from the companion experiments.

### 3.3 Validation Studies

As a parallel effort, we have also pursued validation studies of the combustion and turbulence models being used in the hybrid combustion studies. In our previous report, we presented results of a turbulent reacting shear layer study. In addition, we have performed computations of the methane/air diffusion flame experiment and made detailed comparisons of species and temperature profiles in the combustion zone. These results indicate that the global combustion model is reasonably accurate for representing hydrocarbon combustion. Limited calculations with a more detailed kinetics model are planned for further comparisons.

## 4. Future Plans

In the coming months, we plan to perform computations of the experimental configuration including the details of the forward-facing and backward-facing steps at the head-end and aft-end of the fuel slab. In particular, the step in the aft-end will be varied parametrically in order to gauge its influence on the degree of downstream mixing and overall combustion efficiency. Secondly, further refinements of the radiation model will be made, specifically, through the inclusion of a model for soot production in the flame. The more complete radiation model will enable quantitative evaluation of the effects of mass flow rate, chamber pressure and size scale-up on surface heat fluxes and, therefore, on the regression rates. Finally, we plan on initiating a limited set of unsteady calculations to help shed light on the instability phenomena observed in the experimental slab burner configuration that is currently being tested.

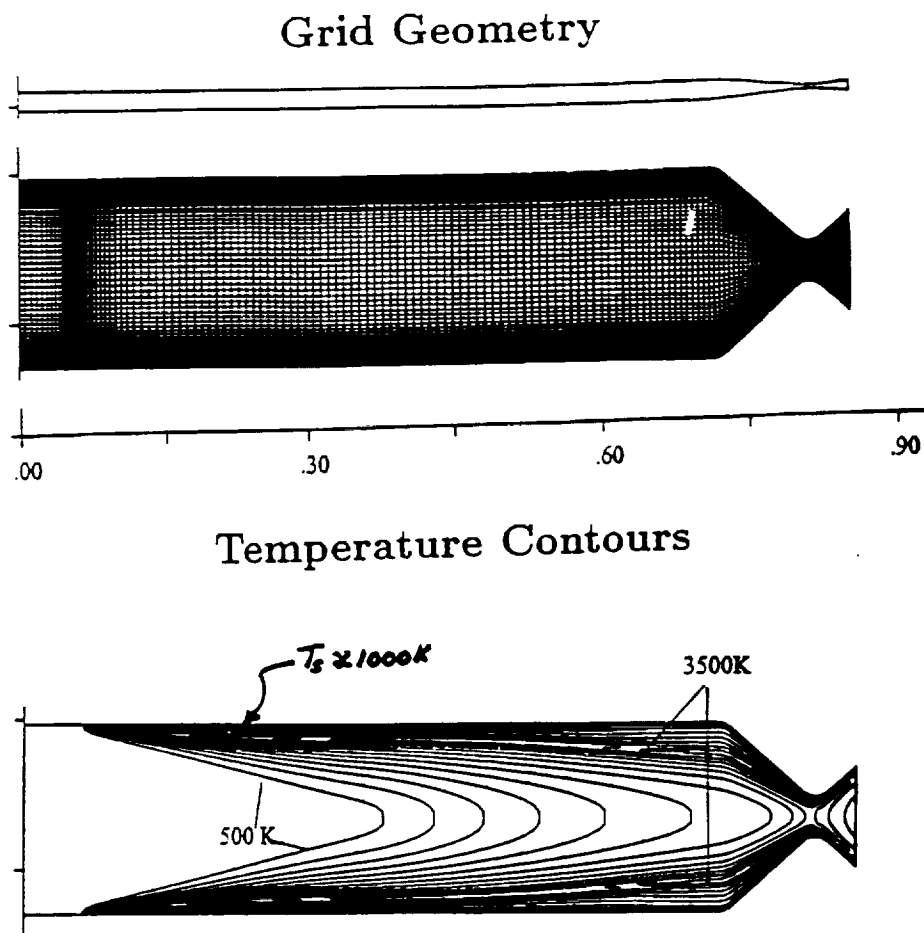


Figure 1 Physical configuration, grid geometry and temperature contours for representative solution. Grid size is  $101 \times 61$ . GOX flow rate is 0.8 lbm/s. Case shown corresponds to about midway through the burn.



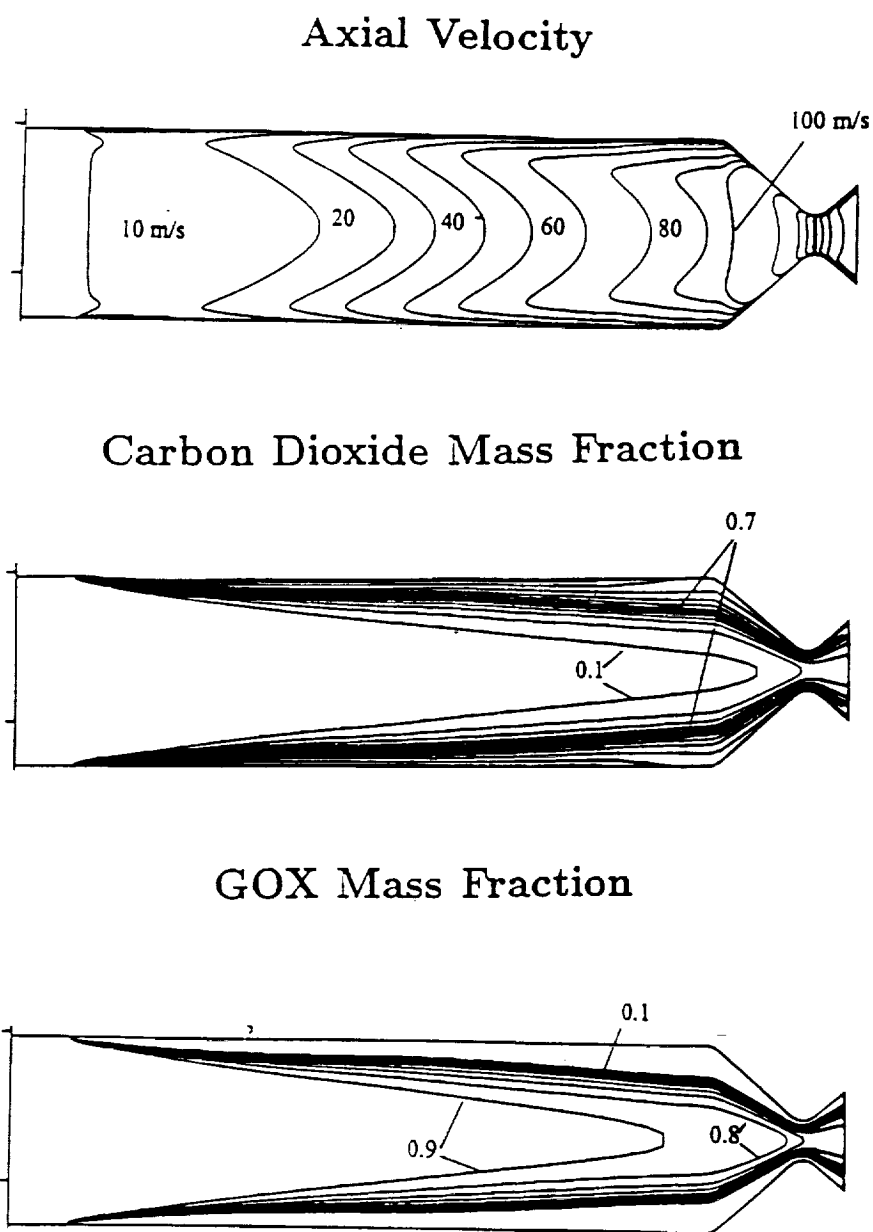


Figure 2 Axial velocity contours, carbon dioxide mass fraction and GOX mass fraction for representative case.

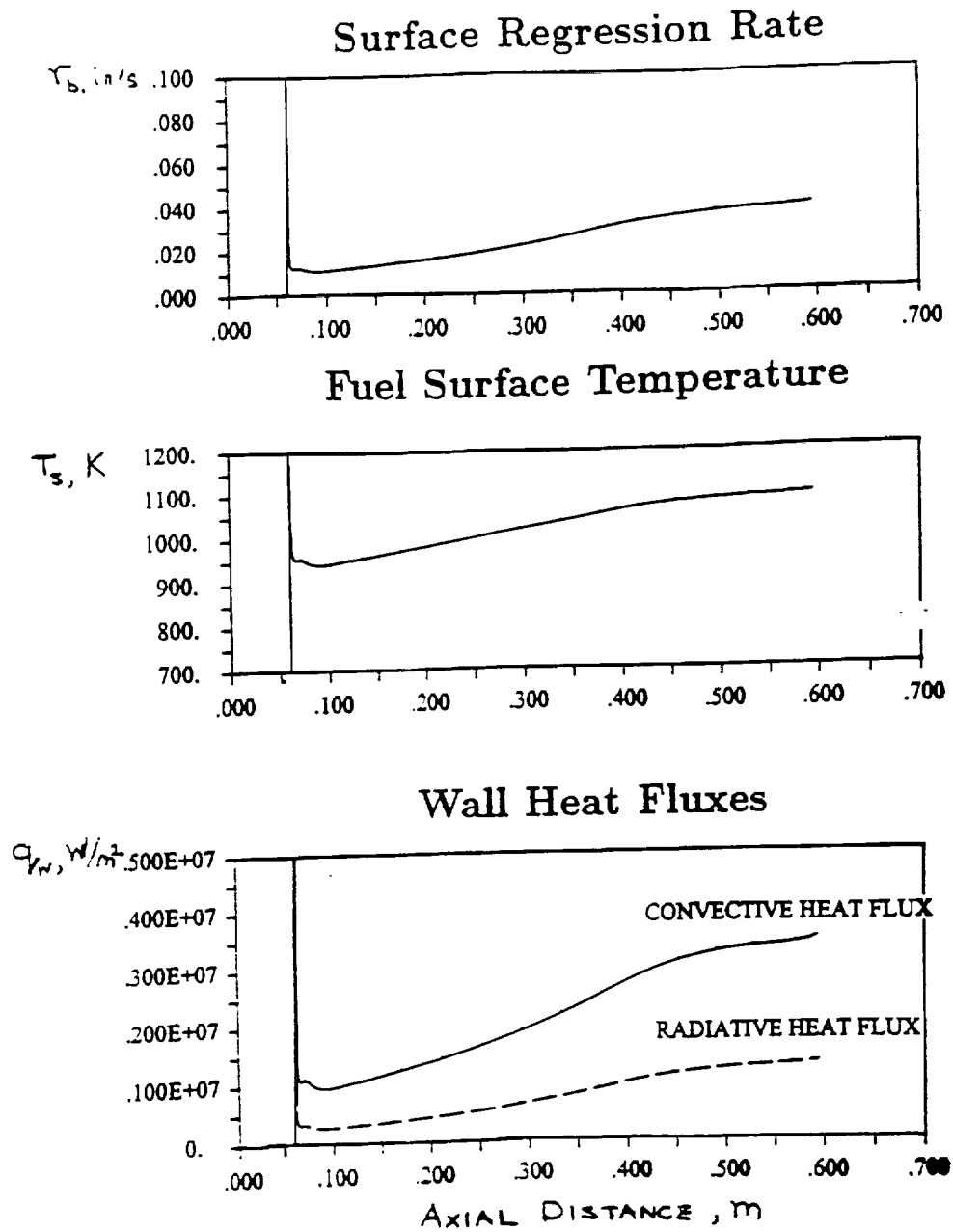


Figure 3 Axial variation of surface regression rate, temperature and heat fluxes for representative case.

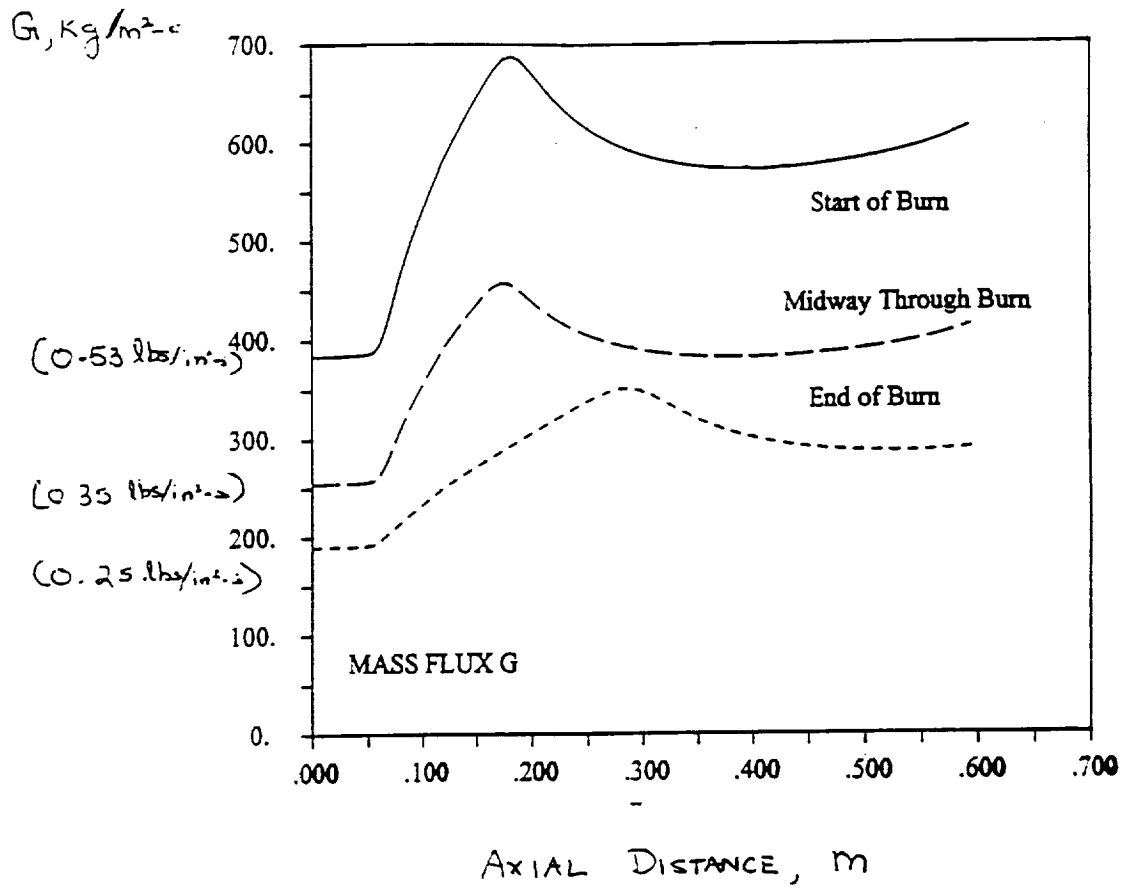


Figure 4 Centerline variation in mass flux as a function of axial location.

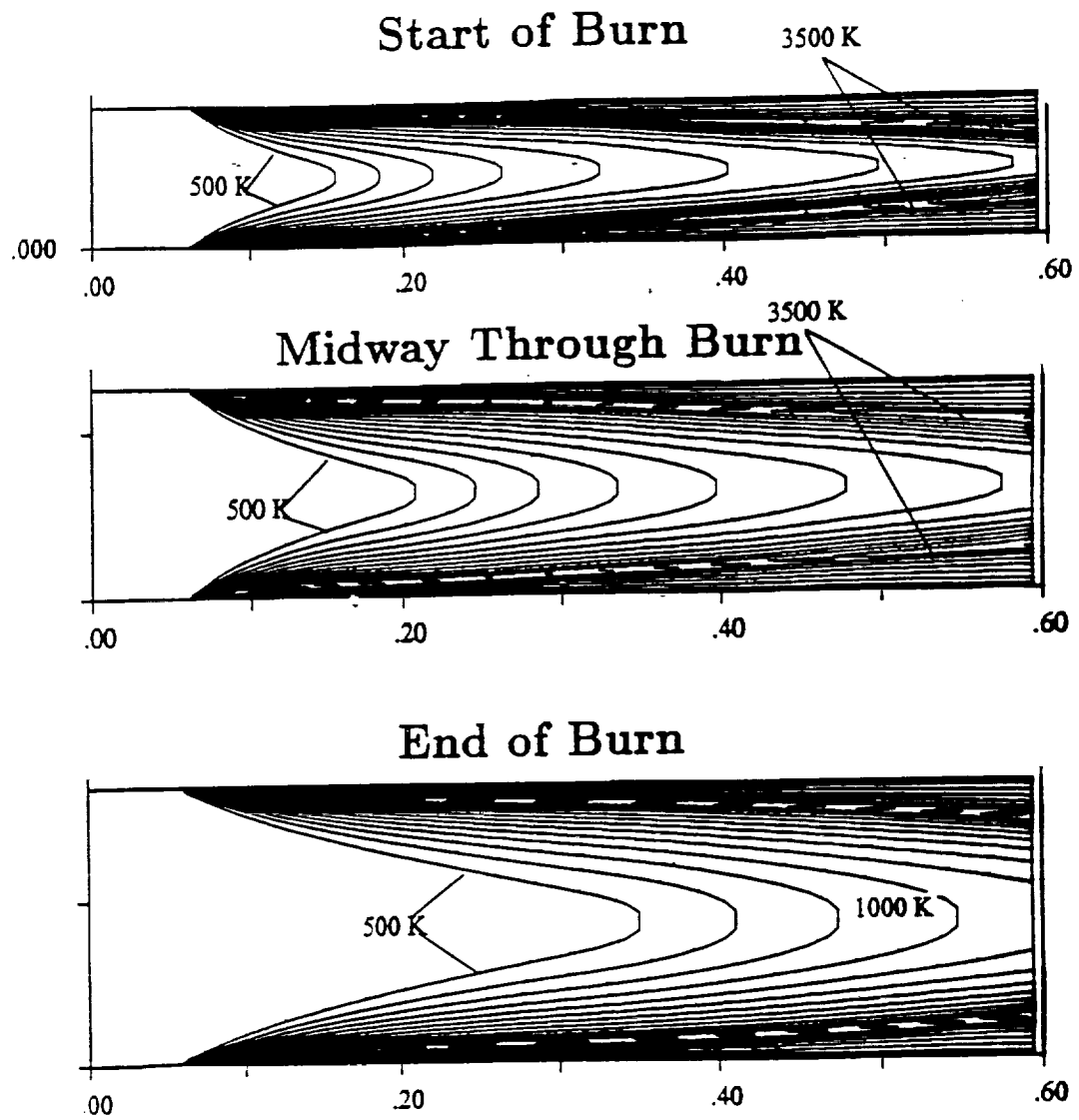


Figure 5 Temperature contours for several stages in the burn.

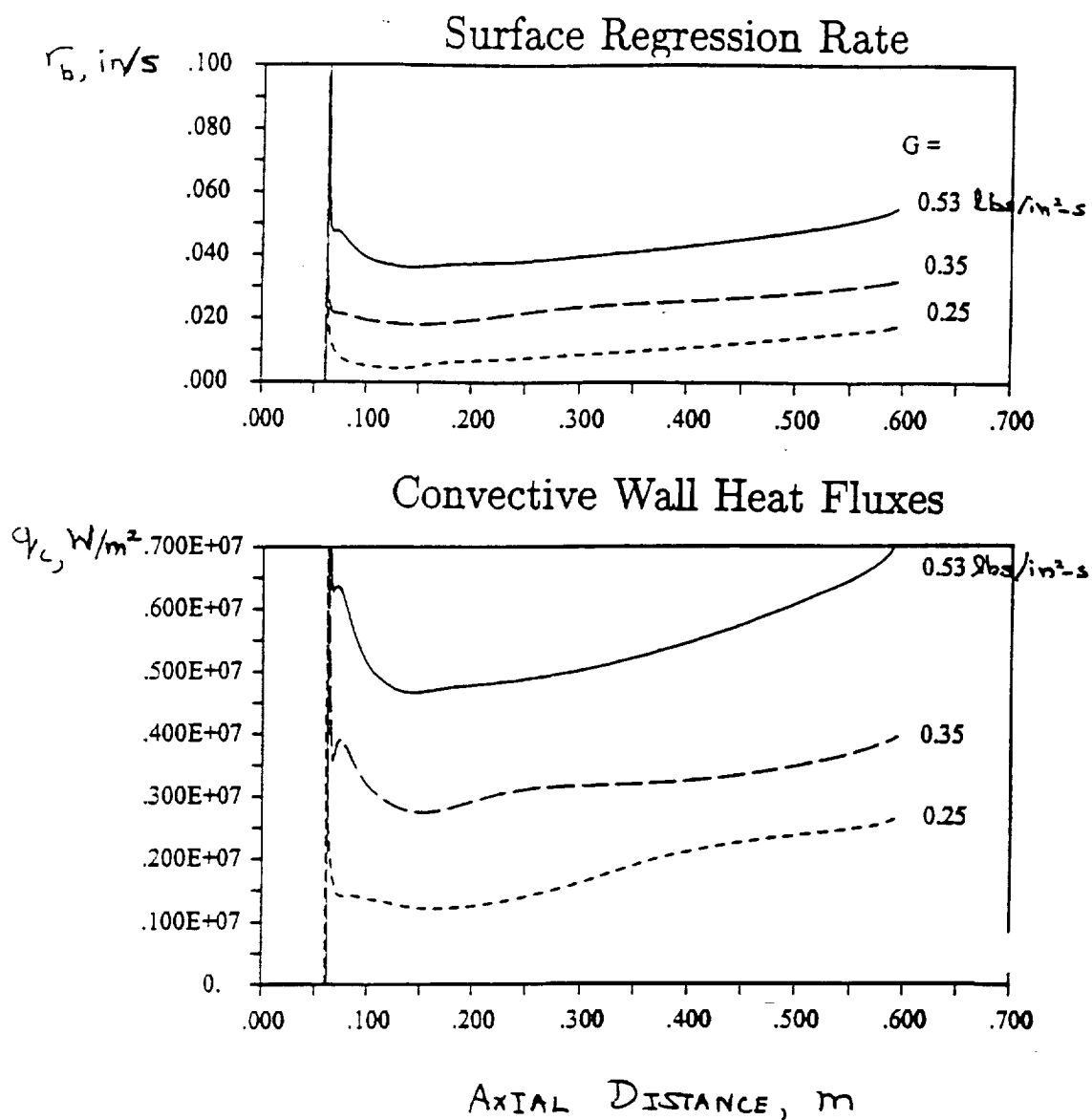


Figure 6 Surface regression rate and convective wall fluxes when radiative transfer in the gas is neglected.

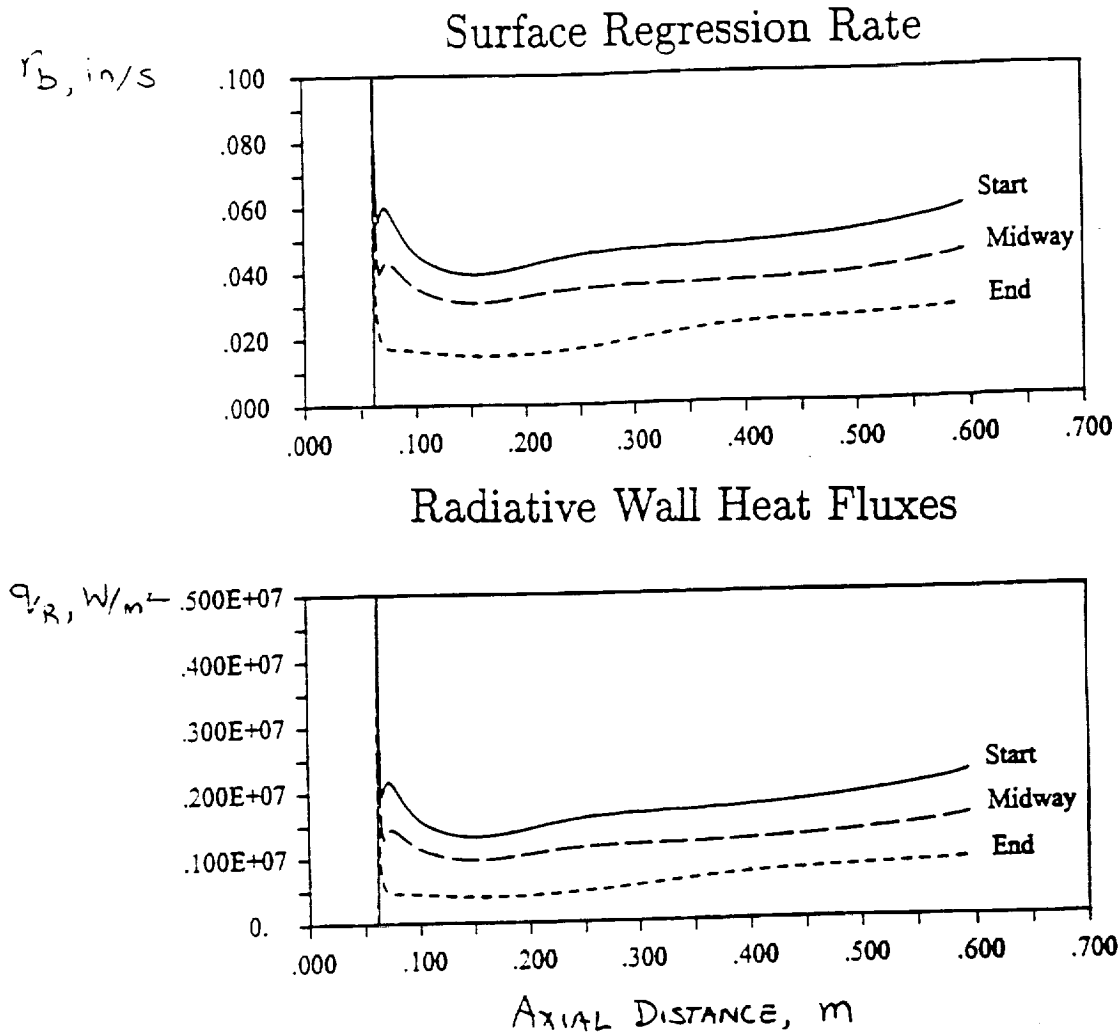
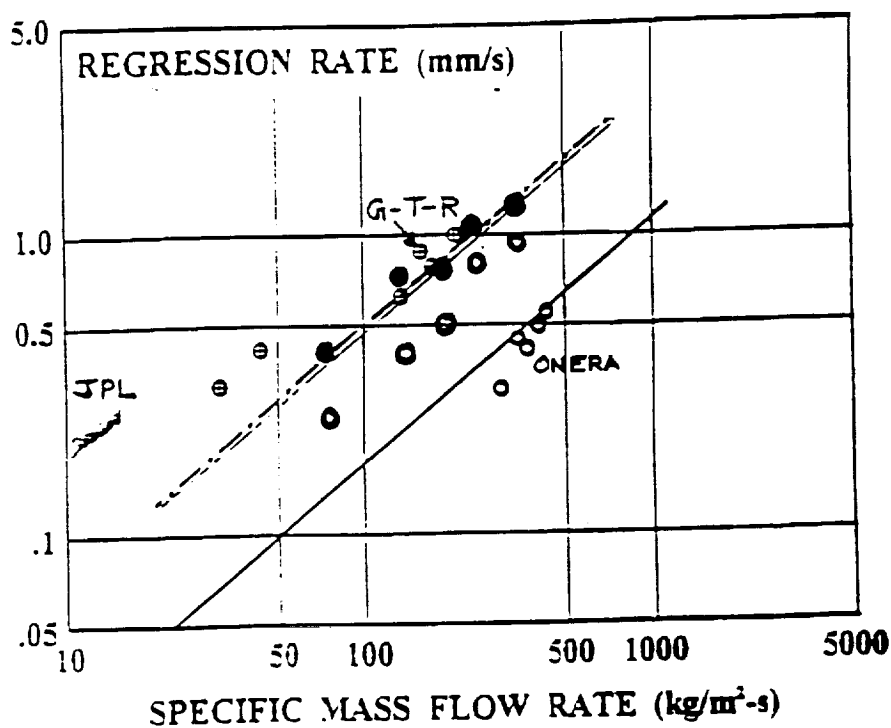


Figure 7 Surface regression rate and radiative wall fluxes when radiation is modeled using the optically thick approximation.



- Current Results with Radiation
- Current Results W/O Radiation

Figure 8 Characterization of fuel surface regression. Comparison with small-scale test data from JPL, General Dynamics-Thiokol-Rocketdyne (G-T-R) and ONERA. Note that ONERA data is for HTPB/air.